▌ **Medicinal Chemistry & Drug Discovery**

Spiro-Indole-Coumarin Hybrids: Synthesis, ADME, DFT, NBO Studies and In Silico Screening through Molecular Docking on DNA G-Quadruplex

Leena Khanna,[a, b] Sugandha Singhal,[b] Subhash C. Jain,[a] and Pankaj Khanna*[a, c]

New series of hybrids were synthesized by combination of 4-hydroxycoumarin with spiro[indol-indazole-thiazolidine]-diones and spiro[indol-pyrazole-thiazolidine]-diones, *via* hitherto unknown Schiff bases. The effects of substituents, such as -F, -Br and -CH₃, on the crucial characteristics pertaining to the hybrids were investigated through computational studies. *In silico* or virtual screening through molecular docking studies on the library of 22 compounds, including reference compounds, precursors, non-hybrid and hybrid derivatives, was performed on DNA G-quadruplex of the human genome. All six freshly synthesized hybrids showed high binding energy as compared to non-hybrids as well as reference compounds. The presence of substituents at 5-position of indole enhanced the binding tendency of the ligand. ADME studies indicated good oral bioavailability and absorption of these compounds. Density

Functional Theory (DFT) calculations of hybrids were done at B3LYP/6-311G++(d,p) level of computation. Their HOMO and LUMO energy plots reflected the presence of high charge transfer and chemical potential. Natural bond order (NBO) calculations predicted hyperconjugative interactions. The Molecular Electrostatic Potential (MEP) surface plots showed possible electrophilic and nucleophilic attacking sites of the hybrids. Compound **10a** (5-fluoro-spiro[indol-indazole-thiazolidine]-dione-coumarin hybrid), on the basis of global reactivity descriptors, was filtered to be chemically most reactive with the highest binding energy of −8.23 kcal/mol with DNA G-quadruplex. The synthesized hybrid coumarin derivatives in correlation with theoretical docking studies validate that hybrid derivatives are more reactive compared to their non-hybrid counterparts.

Introduction

Coumarins or 2*H*-chromen-2-ones constitute an important group of natural products and are known to possess varied activities *viz.* antibacterial, antiallergic, anti-inflammatory, antioxidant, anticoagulant. Among the various coumarins known, O-alkylated coumarins constitute an important group of naturally occurring compounds e.g., **1** (Figure 1) has been isolated from *Mutisia orbignyana*.[1]

The O-alkylated coumarins **2** (Figure 1), have shown antibacterial activity against *Bacillus subtilis* and *E. coli*.[2]

Also, the anticancer activity of coumarin derivatives has been well screened. 6-Brominated coumarin hydrazide-hydrazone derivatives (BCHHD) were found to be more effective against resistant Panc-1 cells than doxorubicin (DOX).[3] Whereas coumarin derivatives having 4,5-dihydropyrazole moiety exhibited as potential telomerase inhibition activity against human gastric cancer cell SGC-7901.[4]

Besides this, indole-2,3-diones when joined using alkyl bridges to different heterocyclic moieties have been known to act as SARS coronavirus 3CL protease inhibitors.[5] Bis-indolinone derivatives having 2,6-disubstituted pyridine core or 1,10-disubstituted phenanthroline core showed high binding with G-quadruplexes as well as antitumor activity.[6]

Similarly, naturally occurring indole alkaloids, Spirotryprostatins A and B obtained from the fermentation broth of *Aspergillus fumigates*, inhibited the G2/M progression cell division in mammalian tsFT210 cells. While synthetically prepared dispiro[3*H*-indole-3,2′-pyrrolidine-3′,3′′-piperidine]-2(1*H*),4′′-diones displayed effective antitumor activities against the cervical cancer cell line (HeLa) more than that of cisplatin.[7]

Fascinatingly, hybrid molecules are generally designed to target simultaneously two different sites with synergistic effects or acting as dual drugs.[8–10] Also, a single molecule carrying multiple pharmacophores acts as a hybrid multifunctional entity and is more useful as each pharmacophore displays diverse modes of action.

Therefore, considering the importance of coumarin and spiro-indoles, we thought of developing their hybrid molecules in anticipation of having better pharmacophoric features and biological profiles. Hence, in vogue of combining more numbers of bioactive moieties in a single molecular framework and continuing our interest in spiro-indoles,[11–16] we thought of synthesizing hybrids of spiro[indol-indazole/pyrazole-thiazolidine]-diones with coumarin.

[a] Dr. L. Khanna, Prof. Dr. S. C. Jain, Dr. P. Khanna
Department of Chemistry, University of Delhi, Delhi 110007 (India)
E-mail: pankajkhanna@andc.du.ac.in
[b] Dr. L. Khanna, S. Singhal
University School of Basic and Applied Sciences, Guru Gobind Singh Indraprastha University, Sector 16-C, Dwarka, New Delhi 110078 (India)
[c] Dr. P. Khanna
Department of Chemistry, Acharya Narendra Dev College, University of Delhi, Kalkaji, New Delhi 110019 (India)

🖳 Supporting information for this article is available on the WWW under https://doi.org/10.1002/slct.201904783

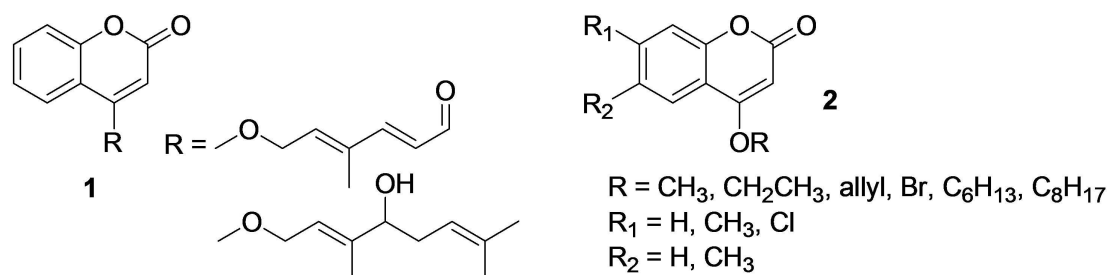R = CH₃, CH₂CH₃, allyl, Br, C₆H₁₃, C₈H₁₇
R₁ = H, CH₃, Cl
R₂ = H, CH₃

Figure 1. Potent O-alkylated coumarin derivatives

Also, there has been no report of these types of potentially active indolyl compounds containing coumarin, thiazolidine and pyrazole moieties in one frame. However, as it was difficult to introduce the coumarin moiety into the spiro-indole already having two bioactive moieties, a literature survey revealed alkyl bridge between any two moieties as a possible route for the preparation of the desired compounds.

All the six new hybrids were characterized using detailed spectroscopic analysis experimentally and theoretically. The computational studies were performed for these six spiro indole-coumarin hybrids, **10a-c** and **12a-c** in order to study their stability and biological potency.

Also, it is well known the fact that the formation of G-quadruplex inside the human body at telomeres can change many cellular functions, inducing apoptosis or may cause cancer. However, the development of synthetic molecules that are able to bind and stabilize these telomeric G-quadruplexes is catching attention nowadays as there are proving as attractive therapy as antitumor agents.[17–19] As we have already discussed that literature revealed both spiro-indoles and coumarin derivatives possessed potent antitumor properties; hence, it can be evaluated in their hybrids also. Thus, in the present study, the biological importance of **22** compounds including six new spiro indole-coumarin hybrids as DNA quadruplex groove binders has been evaluated by performing molecular docking studies on DNA G-quadruplexes of the human genome.

Finally, Density Functional Theory (DFT) calculations, NBO analysis, and MEP plots are drawn for hybrids to prove their chemical reactivity and stability.

Results and Discussion

The reaction of 4-hydroxy-2H-chromen-2-ones (**3**) with 1,6-dibromohexane (**4**) in the presence of NaH in dry DMF at −10°C under inert atmosphere gave a mixture of two compounds **5** and **6** (Scheme 1). These were separated by column chromatography. The compound **5** obtained as white solid, displayed a molecular ion peak at m/z 324 corresponding to the molecular formula $C_{15}H_{17}O_3Br$. The IR spectrum showed characteristic absorption at 1711 cm⁻¹. The absence of absorption for –OH group indicated that alkylation has occurred. Its ¹HNMR spectrum showed signals integrating for aromatic protons of coumarin at δ 7.81 (H-5), δ 7.55 (H-7) and δ 7.28 (H-

6 and H-8). The H-3 proton appeared at δ 5.66 as a singlet. The protons of alkyl group appeared at δ 4.14 (t, OCH₂), δ 3.43 (t, CH₂Br) and as multiplets at δ 1.92 and δ 1.58 for the other four methylenes. ¹³C NMR spectrum displayed the presence of carbonyl carbon at δ 165.3 in addition to carbons at δ 160.9 (C-4), δ 153.1-90.2 (aromatic carbons), δ 69.4 (OCH₂) and δ 34.1 (CH₂Br). The above spectral data confirmed the formation of **5** which was characterized as 4-(6-bromohexyloxy)-2H-chromen-2-ones.

Besides **5**, another compound **6** formed in minor amount in the course of reaction was characterized as (2-oxo-2H-chromen-4-yloxy)-1,1′-(hexanediyl)bis.

The bromide **5** on reaction with 5-fluoro-1H-indol-2,3-dione (**7a**) in the presence of NaH in dry DMF under nitrogen gave a red colored solid **8a** whose molecular ion peak appeared at m/z 409 which corresponded to the molecular formula $C_{23}H_{20}NO_5F$. Its IR spectrum showed the presence of carbonyl peaks at 1735, 1727 and 1709 cm⁻¹. The ¹HNMR spectrum showed aromatic protons of the indole nucleus at δ 7.30 (H-4″ & H-6″) and δ 6.86 (H-7″) besides the protons of coumarin moiety at usual values. The methylenes appeared at δ 4.12 (t, OCH₂), δ 3.74 (NCH₂) as triplets besides the other four methylenes at δ 1.91, δ 1.75 and δ 1.54 as multiplets. The ¹³C NMR spectrum showed characteristic carbonyl at δ 185.1 (C-3″), δ 163.2 (C-2″) and δ 165.9 (C-2), apart from the aromatic and alkyl carbons. The above spectral studies confirmed the formation of 1-[6-(2-oxo-2H-chromen-4-yloxy)hexyl]-5-fluoro-1H-indol-2,3-dione (**8a**).

The reaction of **8a** with 5-aminoindazole in absolute ethanol under refluxing conditions gave a reddish solid **9a**, which displayed molecular ion peak M⁺ at m/z 524 corresponding to the molecular formula $C_{30}H_{25}N_4O_4F$. IR spectrum showed characteristic absorptions at 3259 cm⁻¹ (>NH, indazole) and 1644 cm⁻¹ (C=N) besides other carbonyl bands. ¹HNMR spectrum showed the peaks of indazole as singlets at δ 8.10 (H-3‴) and 7.40 (H-4‴) and as multiplets at δ 7.59 (H-6‴) and δ 7.15 (H-7‴) apart from other protons of coumarin and indole moiety. ¹³C NMR spectrum showed carbons at δ 166.1 (C-2″), δ 162.9 (C-2), δ 162.7 and δ 143.9 (C=N) and aromatic carbons between δ 139.0-109.5 besides alkyl carbons between δ 69.5-26.1. The above spectral studies confirmed the formation of desired Schiff base **9a** characterized as 1-[6-(2-oxo-2H-chromen-4-yloxy)hexyl]-5-fluoro-3-(indazol-5-yl) imino-1H-indol-2-one.
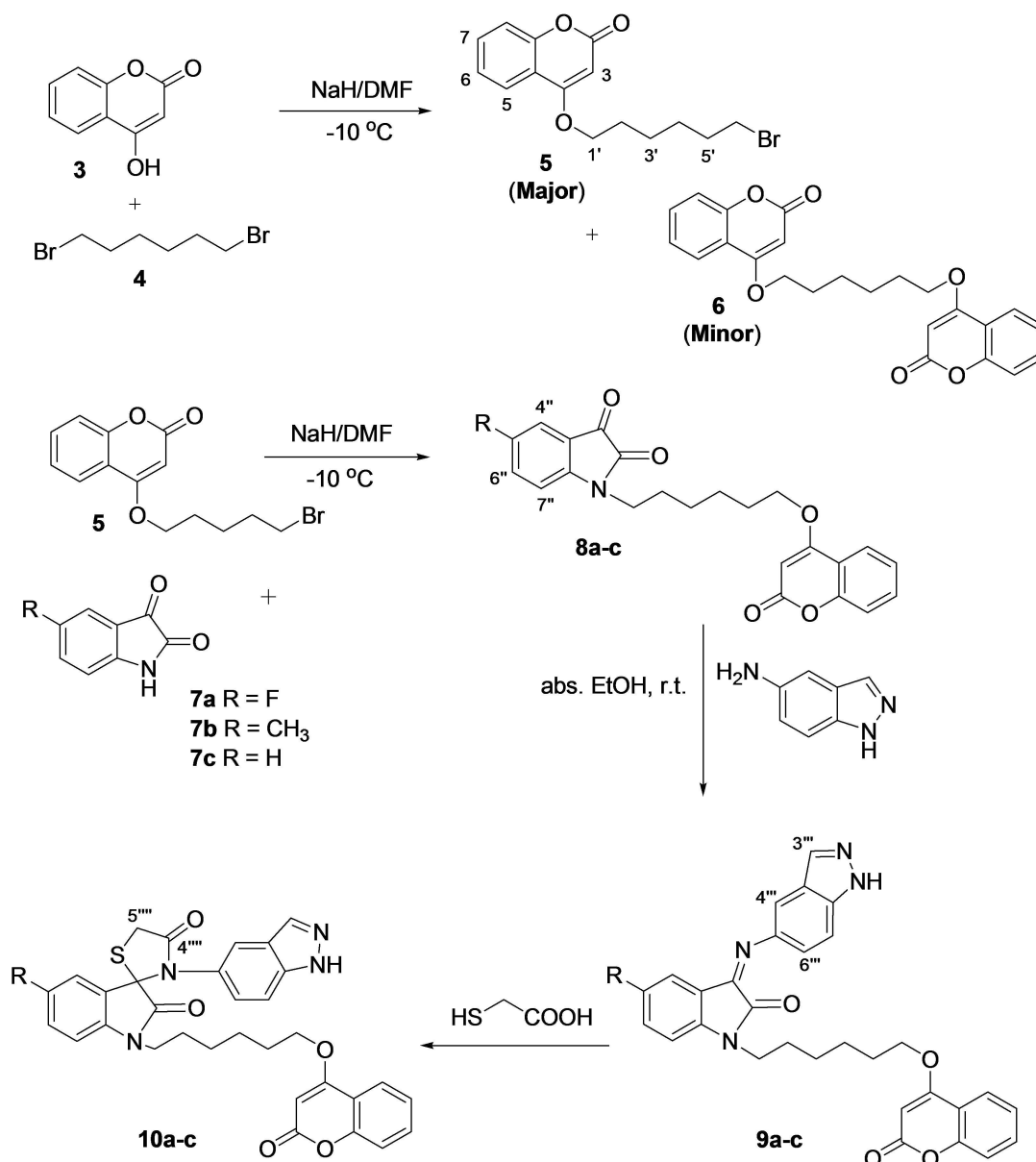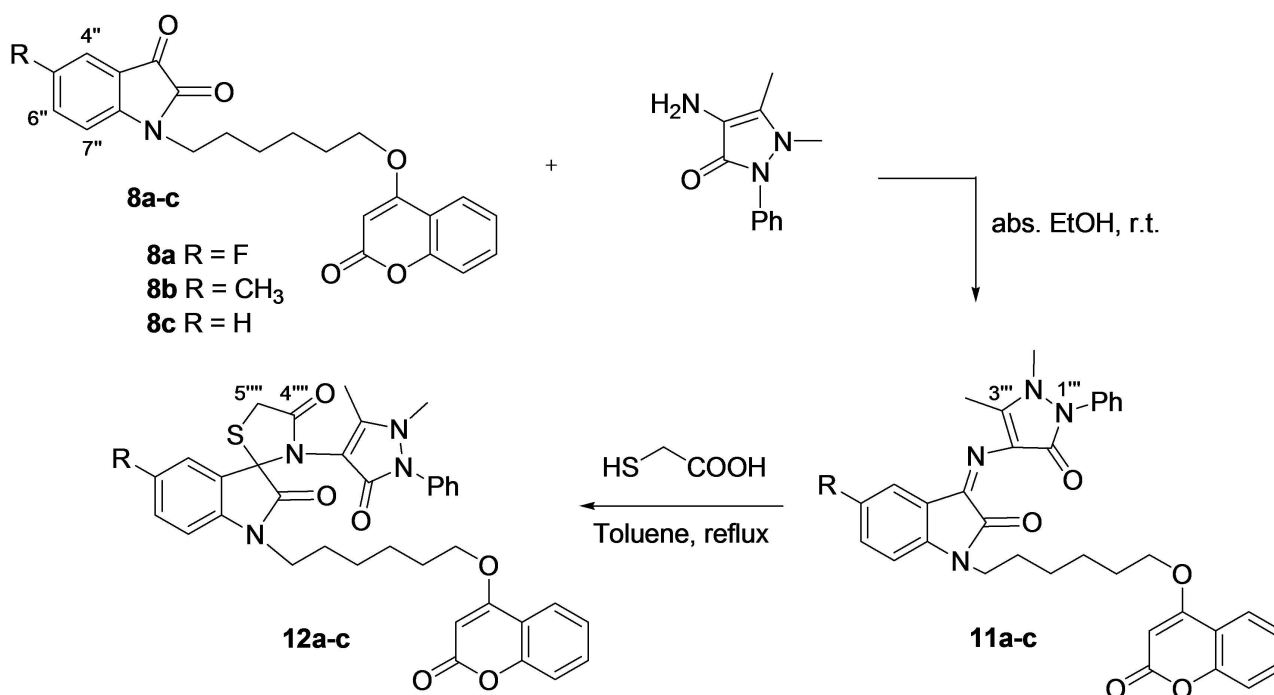
Scheme 1. Synthetic protocol of 1-[6-(2-oxo-2H-chromen-4-yloxy)hexyl]-3'-(indazol-5-yl)spiro[3H-indol-3,2'-thiazolidine]-2,4'-diones

The Schiff base **9a** was reacted with mercaptoacetic acid under refluxing conditions using Dean-Stark apparatus to obtain a new compound **10a**, whose molecular mass was found to be 598 corresponded to the molecular formula $C_{32}H_{27}N_4O_5FS$. The IR spectrum in this compound showed distinct characteristic absorption at 3321 cm^{-1} (>NH, indazole), 1724 cm^{-1} (thiazolidine carbonyl), 1718 cm^{-1} (coumarin carbonyl) and 1681 cm^{-1} (indole carbonyl), thus confirming the cycloaddition. ^{1}H NMR spectrum showed the presence of methylene of thiazolidine as two doublets at δ 4.37 and δ 4.05 besides the usual aromatic protons of indole, indazole and coumarin moieties. The ^{13}C NMR spectrum showed peaks at δ 175.2 (C-4''''), δ 173.3 (C-2''), δ 166.0 (C-2) and δ 33.2 (C-5'''') besides other aromatic and alkyl carbons. The above spectral data confirmed the formation of desired spiro compound **10a**

characterized as 1-[6-(2-oxo-2H-chromen-4-yloxy)hexyl]-3'-(indazol-5-yl)spiro[3H-5-fluoro-indol-3,2'-thiazolidine]-2,4'-dione.

The indol-2,3-dione (**8a**) was also reacted with 4-aminoantipyrine in similar fashion to obtain a red colored solid **11a**, whose molecular ion peak appeared at m/z 594 corresponding to the molecular formula $C_{34}H_{31}N_4O_5F$ (Scheme 2). The IR spectrum showed absorptions at 1725, 1718 and 1641 cm^{-1}. The ^{1}H NMR spectrum showed the peaks at δ 7.50 & δ 7.48 (N-C_6H_5), δ 3.29 (N-CH$_3$) and δ 2.47 (3'''-CH$_3$) of pyrazoline moiety with corresponding integrations, besides the usual protons. The ^{13}C NMR spectrum showed characteristic peaks at δ 145.7 (C=N), δ 36.3 (N-CH$_3$) and δ 11.7 (3'''-CH$_3$). Thus on the basis of the above spectral data **11a** was confirmed as 1-[6-(2-oxo-2H-chromen-4-yloxy)hexyl]-3-(2,3-dimethyl-5-oxo-1-phenyl-3-pyrazolin-4-yl) imino-5-fluoro-1H-indol-2-one.

Scheme 2. Synthetic protocol of 1-[6-(2-oxo-2*H*-chromen-4-yloxy)hexyl]-3′-(2,3-dimethyl-5-oxo-1-phenyl-3-pyrazolin-4-yl)spiro[3*H*-indol-3,2′-thiazolidine]-2,4′-diones

The Schiff base **11 a** was cyclocondensed with mercaptoacetic acid in dry toluene under refluxing conditions using Dean Stark apparatus to afford a new compound **12 a** which gave a molecular ion peak at m/z 668 corresponding to molecular formula $C_{36}H_{33}N_4O_6FS$. The IR spectrum showed peak at 1722 cm^{-1}. The ^1H NMR spectrum showed characteristic peaks of thiazolidine methylenes as two doublets at δ 4.39 and δ 3.83 with coupling constant of 15.0 Hz integrating for one proton each. The ^{13}C NMR spectrum also showed peaks of thiazolidine moiety at δ 172.8 (C-4′′′′) and 32.7 (C-5′′′′) besides peaks of indole, pyrazoline, and coumarins moieties. Thus, on the basis of above spectral data, the desired spiro compound **12 a** was confirmed and characterized as 1-[6-(2-oxo-2*H*-chromen-4-yloxy)hexyl]-3′-(2,3-dimethyl-5-oxo-1-phenyl-3-pyrazolin-4-yl)spiro[3*H*-5-fluoroindol-3,2′-thiazolidine]-2,4′-dione.

The detailed spectroscopic data of all the compounds has been summarized in Supplementary Table 1.

Computational Details

The bioactivity scores and drug likeliness properties were determined using Molinspiration virtual screening online software (www.molinspiration.com). The bioactivity scores for GPCR ligands, ion channel modulator, enzymes, and nuclear receptors were predicted. The physicochemical properties of compounds analyzed using Lipinski's rule (LogP, total polar surface area, molecular weight, number of hydrogen bond donors and acceptors, number of atoms, number of rotatable bonds, etc.). The PreADMET online server was used to calculate pharmacokinetic parameters to determine the oral activity of

Table 1. Binding energies of compounds with DNA G quadruplex		
S.No.	COMPOUND	BINDING ENERGY (kcal/mol)
1.	**10a**	-8.23
2.	**10b**	-7.46
3.	**10c**	-5.92
4.	**12a**	-6.24
5.	**12b**	-6.01
6.	**12c**	-5.03
7.	**13c**	-4.19
8.	**14a**	-4.89
9.	**14b**	-4.78
10.	**14c**	-4.65
11.	**15c**	-4.02
12.	**16a**	-5.14
13.	**16b**	-4.97
14.	**16c**	-4.68
15.	**17**	-5.73
16.	**18**	-4.41
17.	**19**	-4.01
18.	**9c**	-4.43
19.	**11c**	-4.35
20.	**8c**	-5.55
21.	**7c**	-5.43
22.	**3**	-5.02

the compounds. The parameters such as adsorption, distribution, metabolism and excretion were evaluated.

Density Functional Theory (DFT) calculations of compounds were done using exchange functional by Becke,[20] and correlational functional,[21] at B3LYP/6-311G++(d,p) level of computation using Gaussian 09 software.[22,23] The optimized geometries of compounds **10a-c** and **12a-c** are depicted in Figure 2. These were further used as input for frontier orbital
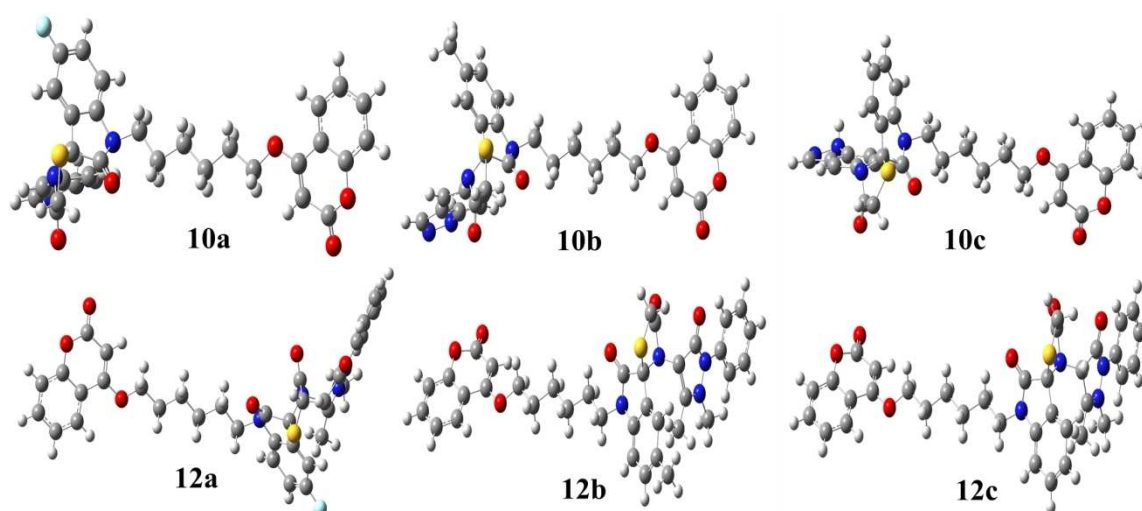
Figure 2. The optimized geometries of compounds **10a-c** and **12a-c**

calculations. The chemical reactivity and chemical potential were predicted from the frontier orbital properties. The atomic charges and hyperconjugative interactions were predicted from natural bond order calculations in vapor phase.

The molecular docking was carried out with Autodock 4.2 program.[24] The crystal structure of G-quadruplex [d(TGGGGT)]4 (PDB ID: 1 s45) was retrieved from the protein data bank (www.rcsb.org). The DNA was prepared by adding polar hydrogens, Kollman united atom charges and solvation parameters. The ligand files were prepared using Gasteiger charge assignment and merging non-polar hydrogens. The grid dimensions in x, y and z directions were kept at 60, 60 and 60 Å respectively. Lamarckian Genetic Algorithm (LGA) method was used for the best conformer search. The docked poses were visualized using Discovery Studio Visualizer 2017.

In silico screening through Molecular Docking

Nowadays, docking is proven to be a highly important technique, useful to predict the interaction of small ligands with biological macromolecules. Therefore in the present work,

about **22** compounds, including newly synthesized spiro-indole hybrids **10a-c** & **12a-c** and Schiff bases (**9c** & **11c**), their non-hybrid spiro-indoles (**14a-c** & **16a-c**) and Schiff bases (**13c** & **15c**) (Figure 3),[16] and three reference compounds (Figure 4),[18,19,25] were correlated with each other on the basis of their DNA G quadruplex binding affinity via Molecular docking as an in silico tool.

All 22 compounds were docked with G-quadruplex [d(TGGGGT)]4 (**PDB ID: 1s45**) and their calculated binding energies are summarized in Table 1. In each case, the best favorable binding pose was selected from the docked structures, and binding energies were calculated.

The data was interpreted by plotting graphs of various compounds versus binding energies. The hybrid compounds were compared with their non-hybrid counterparts to look insight into the influence of coumarin moiety on their activity (Figure 5).

Similarly, the results also compare substitution at 5-position of isatin in spiro-indoles, it was noteworthy that both CH_3 and F were showing an increase in binding interactions, although fluorine was found to be the best (Figure 6).
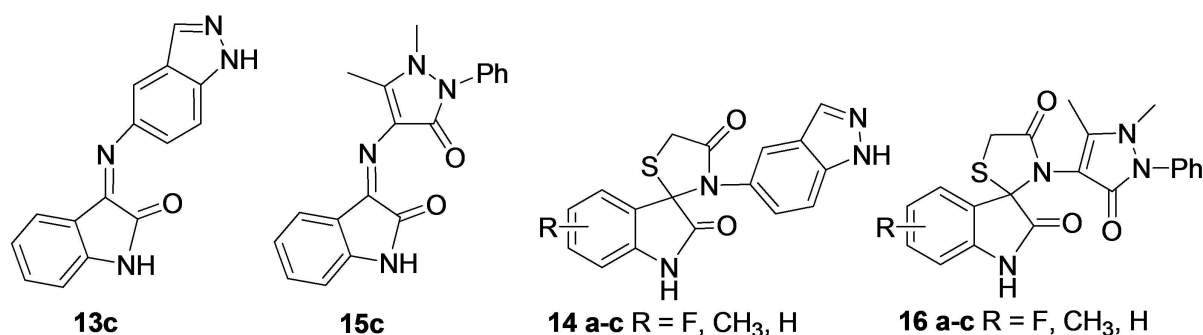

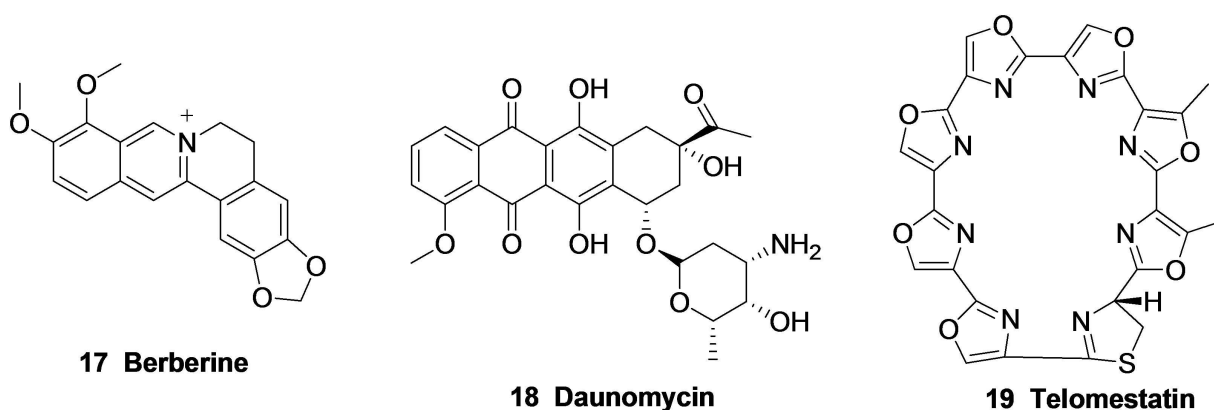**Figure 3.** Non-hybrid Schiff bases and Spiro-indoles

17 Berberine

18 Daunomycin

19 Telomestatin
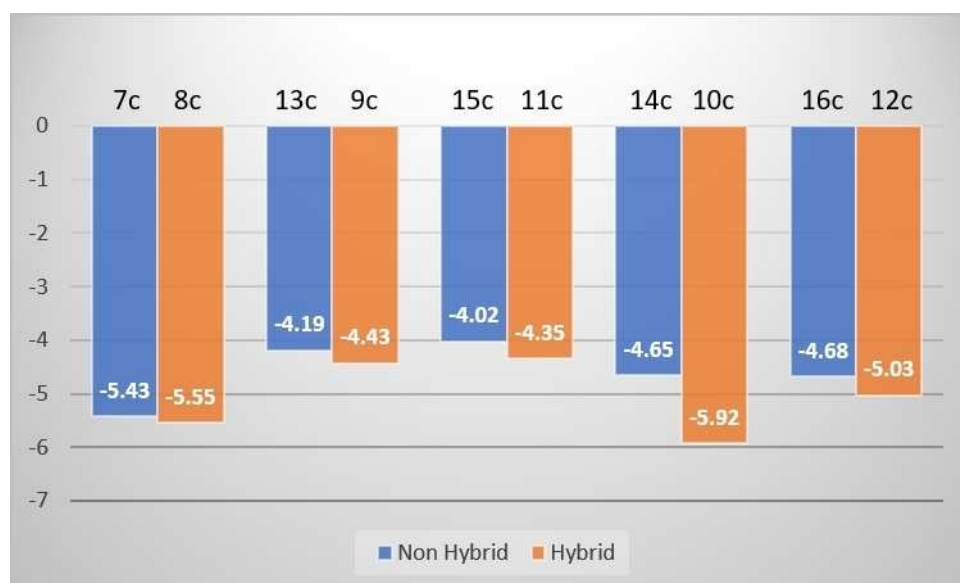
Figure 4. Reference compounds

Figure 5. Comparison of hybrid vs non-hybrid compounds w.r.t. binding energy of G-quadruplex

Table 1 also shows all six newly synthesized spiro indole-coumarin hybrids **10a-c** and **12a-c** are having high binding energy as compared to intermediary Schiff bases, isatin, their non-hybrid counterparts and the reference compounds. However, **10a** is found to be the best binding ligand.

Also, our motive behind using six carbon long chain for hooking up coumarin moiety with spiro-indoles was to enhance their lipophilicity and to provide flexibility to the molecule, which helped it to bind well with DNA G quadruplex.

The compound **10a** binds perfectly to the wide groove of G-quadruplex with binding energy −8.23 kcal/mol. The NH hydrogen atom of pyrazole ring forms hydrogen bond with oxygen atom of DG403 residue (G3). The oxygen atom of thiazolidinone nucleus forms conventional hydrogen bond with hydrogen atoms of DG513 residue (G4) (Figure 7). The aromatic ring of coumarin forms pi-anion interaction with oxygen atom of DG843 residue (G7). The pyrazole ring forms pi-anion interaction with oxygen atom of DG403 residue (G3)

(Figure 8). The indazole ring forms pi-lone pair interactions with DG515 and DG403 residue (G3). The aromatic ring of DT731 residue (G6) depicts pi-sulfur interaction with sulfur atom of thiazolidinone nucleus (Figure 9).

ADME studies and physicochemical parameters

The compound is considered active if bioactivity score is > 0, moderately active if score between −5.0-0.0, and inactive if score is < -5.0. All the compounds depicted good bioactivity scores (Table 2). The ADME parameters were within the permissible limits indicating good oral bioavailability of the compounds (Table 3). The HIA (human intestinal absorption) values of $> 90\%$ indicated good oral absorption. The physicochemical properties values such as number of hydrogen bond donors, acceptors, rotatable bonds, and TPSA were also in well agreement (Table 4). Thus, all the six coumaryl spiro-indoles
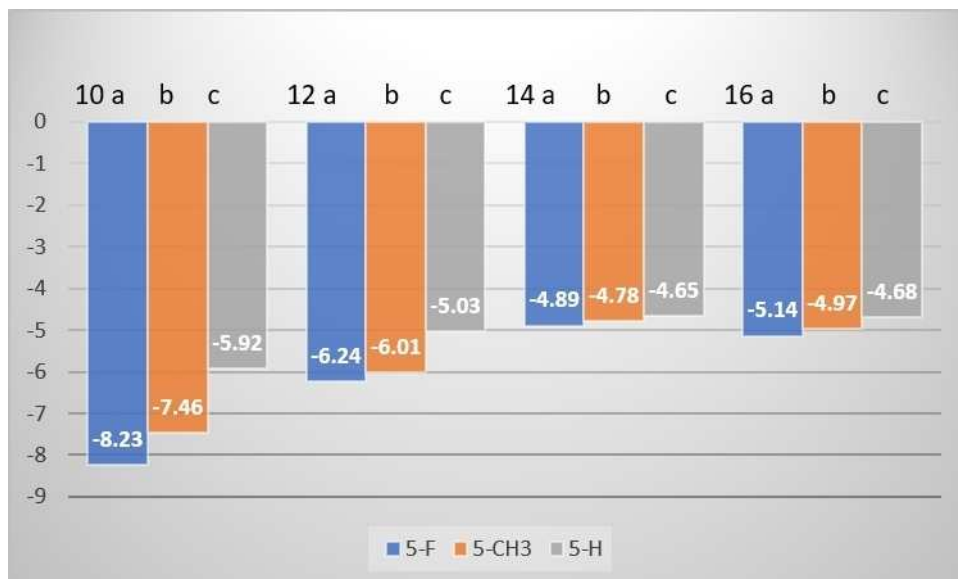
Figure 6. Effect of 5-substitution in the hybrid & non-hybrid spiro-indoles on the binding energy of G-quadruplex
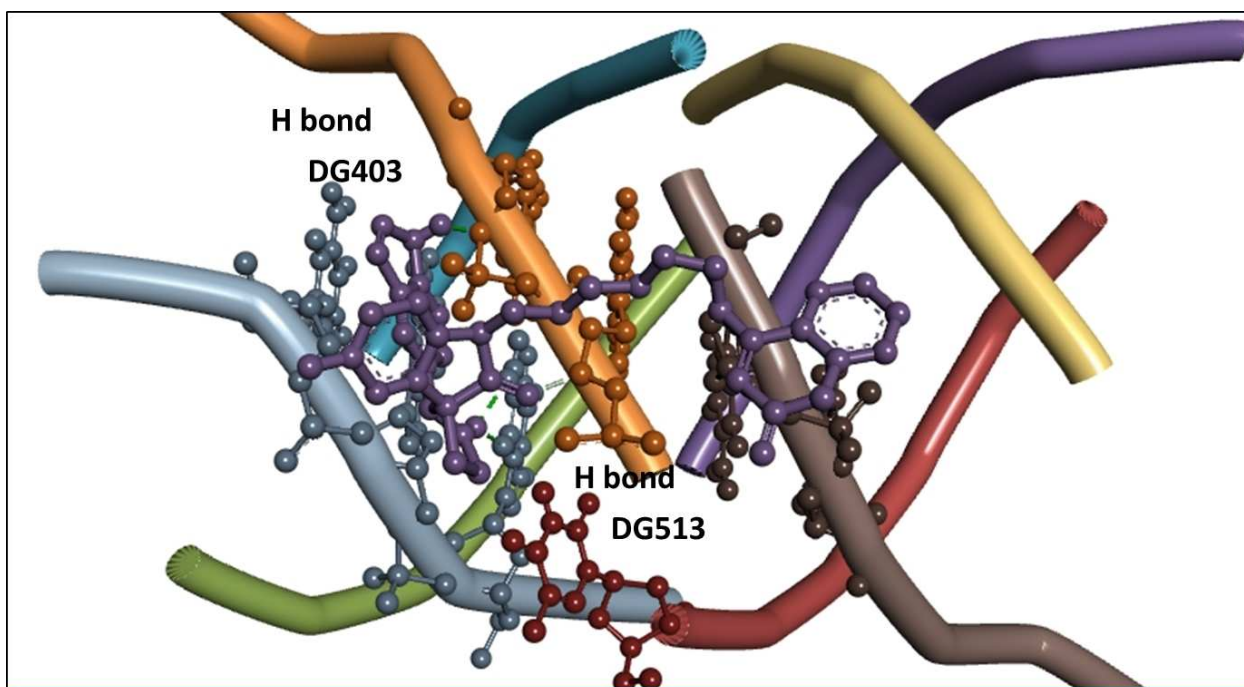

Figure 7. Docked pose of compound 10a showing H-bond interactions with G-quadruplex (PDBID:1s45)

| Table 2. List of bioactivity score of ligands **10**(**a-c**) and **12**(**a-c**)						
Compound	Bioactivity Score Parameters					
	GPCR Ligand	Ion channel modulator	Kinase inhibitor	Nuclear Receptor Ligand	Protease Inhibitor	Enzyme Inhibitor
10a (5F)	-0.43	-0.83	-0.62	-0.70	-0.34	-0.53
10b (5CH$_3$)	-0.46	-0.87	-0.67	-0.73	-0.36	-0.56
10c (H)	-0.40	-0.74	-0.59	-0.66	-0.33	-0.47
12a (5F)	-1.03	-1.82	-1.54	-1.57	-0.85	-1.19
12b (5CH$_3$)	-1.05	-1.85	-1.57	-1.59	-0.86	-1.21
12c (H)	-0.95	-1.69	-1.45	-1.47	-0.80	-1.08
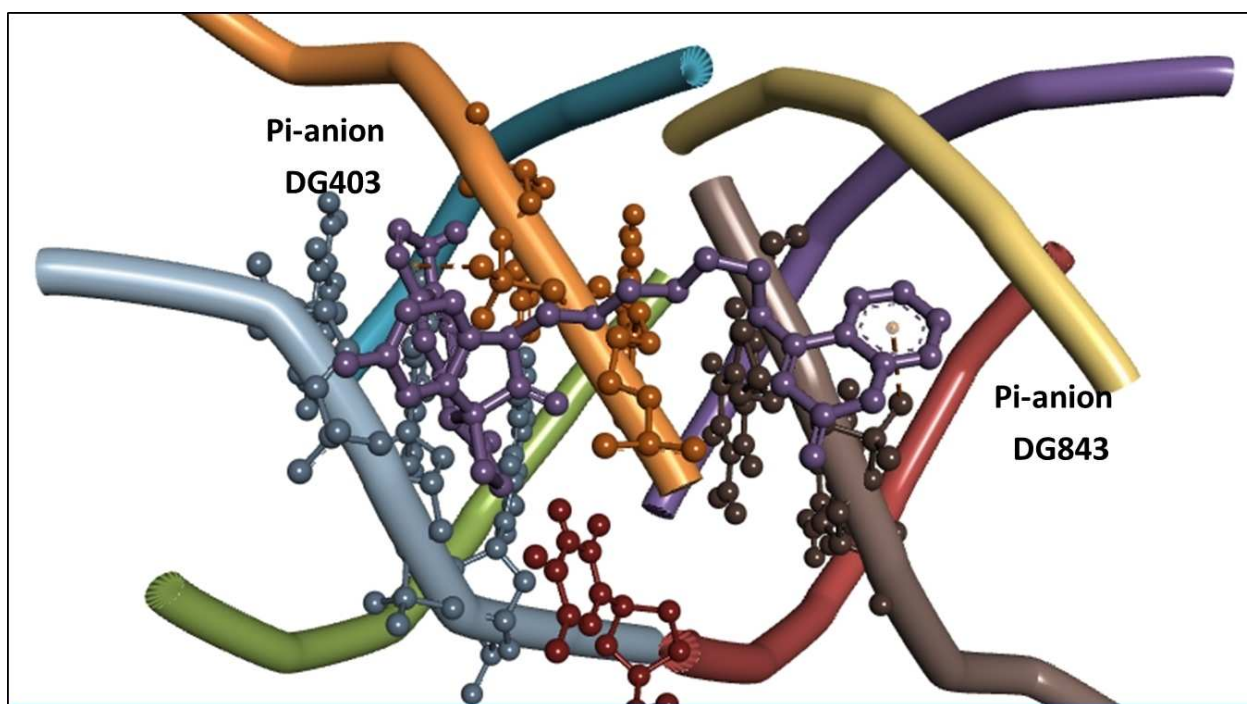
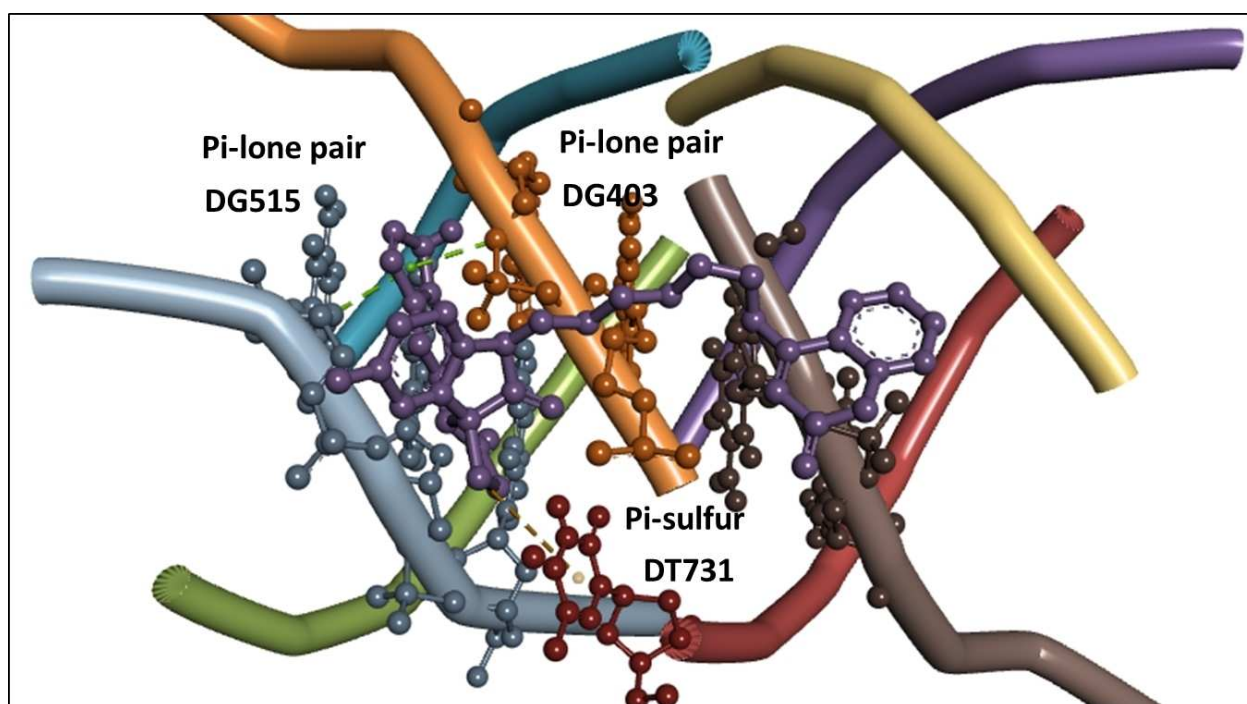**Figure 8.** Docked pose of compound 10a showing pi-anion interactions with G-quadruplex (PDBID:1s45)

Figure 9. Docked pose of compound 10a showing pi-lone pair and pi-sulfur interactions with G-quadruplex (PDBID:1s45).

have shown good overall bioactivity, oral availability despite 2 violations to Lipinski's rule.

Frontier Orbital Calculations

The frontier orbitals HOMO (highest occupied molecular orbital) and LUMO (lowest unoccupied molecular orbital) energies provide significant insight into reactivity and active

Table 3. *In silico* ADME properties of compounds **10(a-c)** and **12(a-c)**

Compound	Log Po/Wa	Log Sb	Caco2c	BBBe	HIA	MDCK	PPB	Skin Permeability
10a (5F)	5.2266	-8.0758	21.9070	0.0391	96.1044	0.1383	96.8633	-3.9088
10b (5CH$_3$)	5.5759	-8.2796	22.6734	0.0525	96.2313	0.2161	94.1648	-3.5218
10c (H)	5.0507	-7.7532	22.1016	0.0321	96.0940	0.4169	92.4385	-3.7437
12a (5F)	5.2770	-8.3489	30.6027	0.5239	98.0533	0.1121	100	-2.8493
12b (5CH$_3$)	4.9277	-8.3286	30.9628	0.4282	98.1455	0.0679	100	-3.2169
12c (H)	4.7518	-7.8224	29.8358	0.3659	98.1543	0.1900	100	-2.8338

Table 4. Physicochemical descriptors for compounds **10(a-c)** and **12(a-c)**

COMPOUND			PROPERTY						
	Log P	TPSA	Natoms	MW	nOH	nOHNH	Nviolations	Nrotb	Volume
10a (5F)	5.67	108.75	43	598.66	9	1	2	9	504.24
10b (5CH$_3$)	5.95	108.75	43	594.69	9	1	2	9	515.87
10c (H)	5.53	108.75	42	580.67	9	1	2	9	499.31
12a (5F)	5.39	107.00	48	668.75	10	0	2	10	573.66
12b (5CH$_3$)	5.67	107.00	48	664.78	10	0	2	10	585.29
12c (H)	5.25	107.00	47	650.76	10	0	2	10	568.73

site of the compounds. The negative chemical potential values indicate the spontaneous decomposition of compounds. The HOMO and LUMO energies and global reactivity descriptors are given in Table 5. The lower energy gap value implies higher chemical reactivity. Using the Koopman's theorem the I and A values can be correlated with Frontier orbitals by the relation:

$$I = -E_{HOMO} \text{ and } A = -E_{LUMO}.^{[26]}$$

The global reactivity descriptors chemical hardness (η), chemical potential (μ), electronegativity (χ) and electrophilicity index (ω) described by Parr,[27] and Pearson,[28] are calculated using equations:[29]

The hardness is given by $\eta = (I - A)/2$ (1)

The chemical potential is given by $\mu = -(I + A)/2$ (2)

The electronegativity is given by $\chi = (I + A)/2$ (3)

The electrophilicity index is given by $\omega = \mu^2/2\eta$ (4)

Compound **10a** having fluoro substituent has the lowest energy gap value; therefore, it is more polarizable and has higher chemical reactivity, low kinetic stability and thus considered as soft molecule among 10a-c series. Similarly,

compound **12a** has the lowest energy gap value among series 12a-c rendering it more polarizable with higher chemical reactivity, and lower kinetic stability. The HOMO-LUMO plots of compounds **10a-c** and **12a-c** are shown in Figure 10.

Natural Bond Orbital Analysis (NBO):

NBO analysis provides information regarding atomic charges in molecular system including conjugative interactions or charge transfer.

Reed and Weinhold performed the NBO calculation,[30] showing that hyperconjugation stabilizes due to the delocalization of electron density to neighboring electron deficient orbital (non-Lewis type NBO) from filled Lewis type NBO. Also, for each donor NBO (*i*) and acceptor NBO (*j*), the stabilization energy can be described by means of second-order perturbation interaction energy E(2) which is given using following equation:

$$E(2) = \Delta Eij = qi\frac{(Fij)2}{Ej - Ei}$$ (5)

where q_i is the donor orbital occupancy, Ei, Ej are the diagonal elements, Fij is the off diagonal NBO Fock matrix element.[31] The NBO analysis was performed at B3LYP/6-311++G(d,p) basis set to estimate the nature of bonds.

Table 5. Frontier orbital energies, global reactivity descriptors of compounds **10(a-c)** and **12(a-c)**

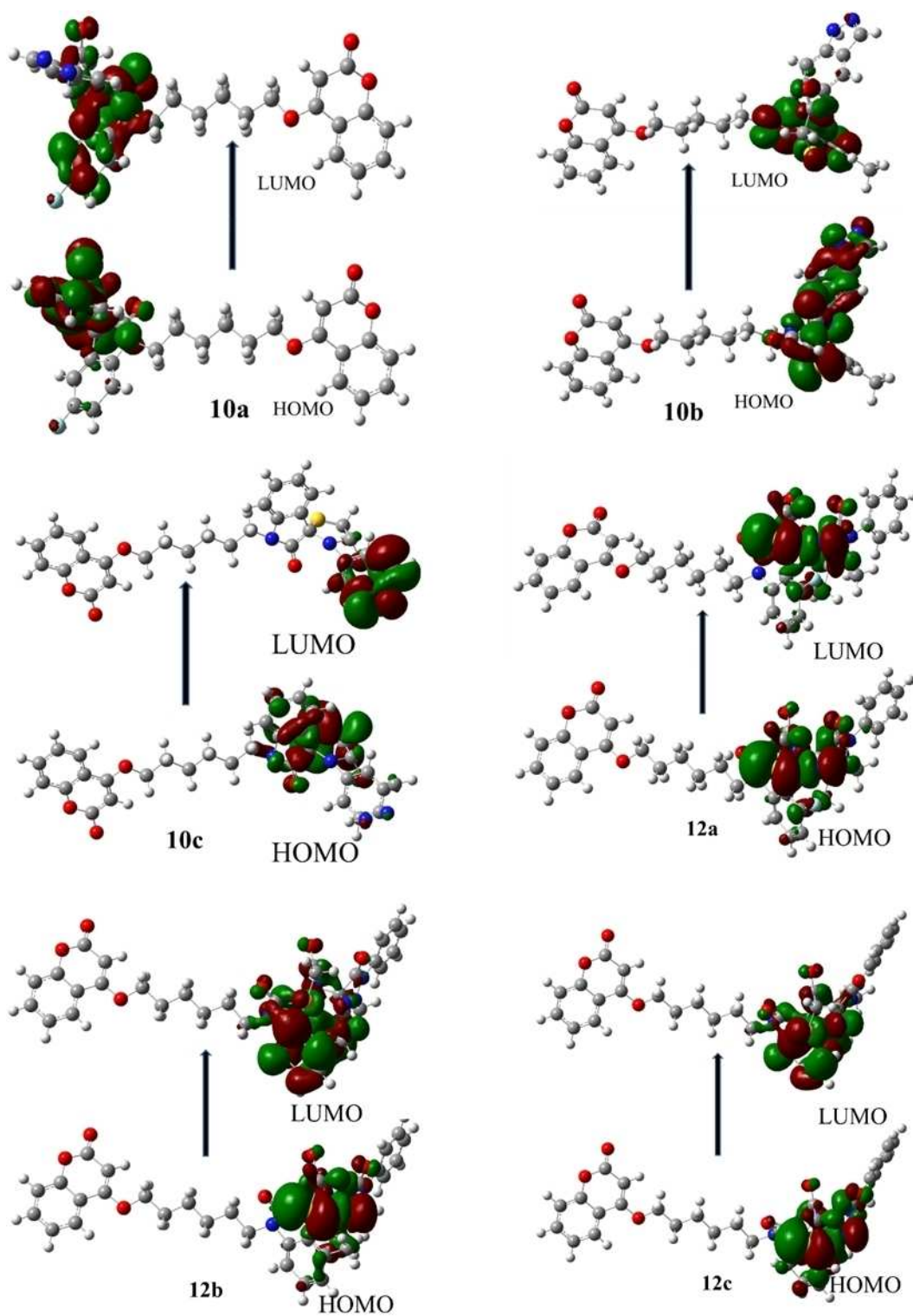| COMPOUND	E$_{HOMO}$	E$_{LUMO}$	Energy Gap	μ	η	X	ω
10a	-0.1334	-0.0335	0.0999	-0.0499	0.0834	0.0499	0.0166
10b	-0.1345	-0.0314	0.1031	-0.0515	0.0829	0.0515	0.0149
10c	-0.1354	-0.0304	0.1050	-0.0525	0.0829	0.0525	0.0166
12a	-0.0581	-0.0391	0.0190	-0.0095	0.0486	0.0095	0.0009
12b	-0.0579	-0.0382	0.0197	-0.0098	0.0480	0.0098	0.0010
12c	-0.0600	-0.0331	0.0269	-0.0134	0.0465	0.0134	0.0019

Figure 10. HOMO-LUMO plots of compounds **10a-c** and **12a-c**

The second order perturbation theory analysis of compound **10a** (Figure 11) is given in Table 6. The major interactions include LP(N17) to σ*(C22-H26), LP(O68) to σ*(C58-O67), and LP(O19) to σ* (C11-N15) with stabilization energies 55.87, 41.06, 33.97 kJ/mol respectively.

The intramolecular hyperconjugative interactions are formed due to orbital overlap between π*(C20-C21) and π* (C22-C25), π*(C20-C21) and π*(C23-C27), and π*(C57-C62) and π*(C60-C63) with respective highest stabilization energies 188.00, 170.20, 182.00 kcal/mol. The high values of E2 indicate

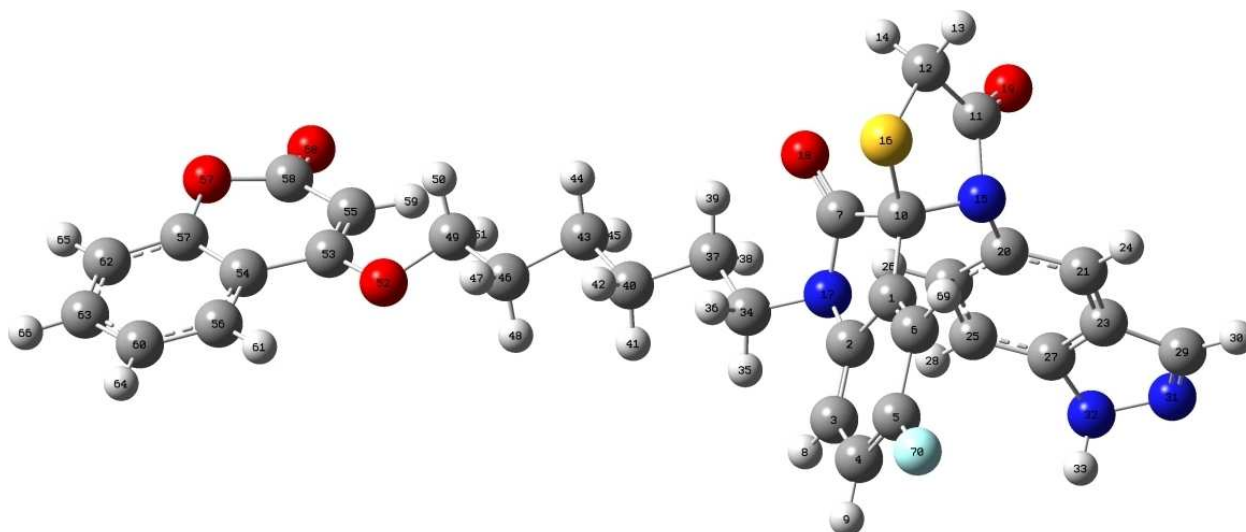**Figure 11.** Labelled structure of **10a**

Donor (i)	Acceptor (j)	E(2) kcal/mol	E(j)-E(i) a.u	F(i,j) a.u	Donor (i)	Acceptor (j)	E(2) kcal/mol	E(j)-E(i) a.u	F(i,j) a.u
σ(C20-C21)	σ*(C22-C25)	22.03	0.30	0.072	σ(C22-C25)	σ*(C23-C27)	24.18	0.28	0.076
σ(C57-C62)	σ*(C60-C63)	21.11	0.30	0.071	σ(C60-C63)	σ*(C54-C56)	23.29	0.28	0.072
LP(N17)	π*(C2-C3)	10.70	0.41	0.059	LP(N15)	π*(C11-O19)	13.84	0.40	0.067
LP(O18)	σ*(C7-N17)	23.99	0.52	0.100	LP(N17)	σ*(C22-H26)	55.87	0.91	0.209
LP(O19)	σ*(C11-C12)	24.04	0.50	0.100	LP(O18)	σ*(C12-C13)	33.04	0.48	0.114
LP(O52)	π*(C53-C55)	31.78	0.29	0.087	LP(O19)	σ*(C7-O19)	33.97	0.48	0.115
LP(O67)	π*(C58-O68)	31.37	0.29	0.085	LP(O67)	π*(C57-C62)	28.60	0.29	0.082
LP(O68)	σ*(C55-O58)	21.81	0.52	0.097	LP(O68)	π*(C55-C58)	21.81	0.52	0.097
LP(F70)	σ*(C5-C6)	11.75	0.64	0.078	LP(O68)	σ*(C58-O67)	41.06	0.42	0.118
π*(C20-C21)	π*(C22-C25)	188.00	0.01	0.076	LP(F70)	π*(C4-C5)	34.28	0.33	0.098
π*(C57-C62)	π*(C60-C63)	182.00	0.01	0.077	π*(C20-C21)	π*(C23-C27)	170.20	0.02	0.083

Table 6. Second order perturbation analysis of the interaction between donor and acceptor orbitals of compound **10a** calculated at B3LYP/6-311++G(d,p)

significant amount of delocalisation involving anti bond orbitals giving non-Lewis NBOs. Detailed data is given in Supplementary Table 2.

Similarly, the second order perturbation theory analysis for compound **12a** (Figure 12) is given in Table 7. The intramolecular hyperconjugative interactions are formed due to anti bond orbital overlap between π*(C43-C48) and π*(C46-C49), π*
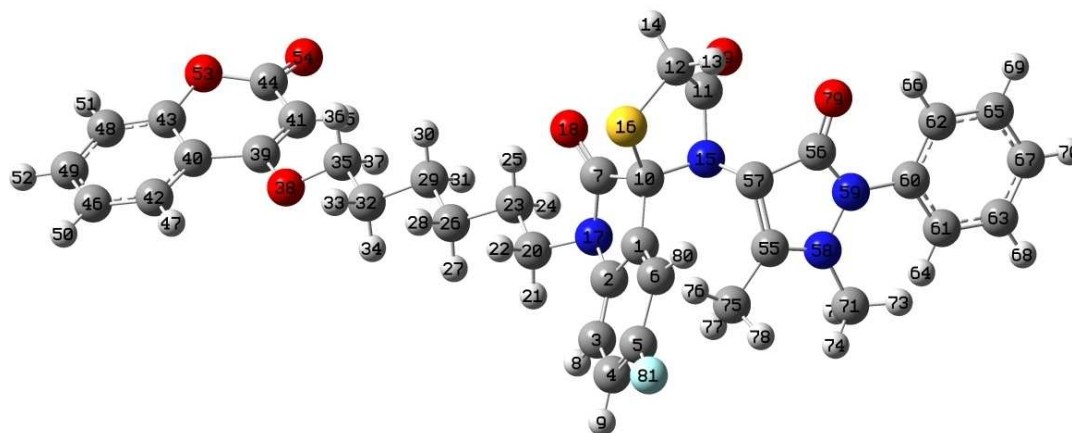

Figure 12. Labelled structure of **12a**

Table 7. Second order perturbation analysis of the interaction between donor and acceptor orbitals of compound **12a** calculated at B3LYP/6-311++G(d,p)

Donor (i)	Acceptor (j)	E(2) kcal/mol	E(j)-E(i) a.u	F(i,j) a.u	Donor (i)	Acceptor (j)	E(2) kcal/mol	E(j)-E(i) a.u	F(i,j) a.u
σ(C75-H76)	π*(C1-C6)	27.77	0.59	0.167	π(C1-C6)	σ*(C75-H76)	54.38	0.93	0.292
LP(O18)	σ* (C7-N17)	16.53	0.48	0.114	LP(O19)	σ* (C11-C12)	11.94	0.53	0.102
LP(O19)	σ* (C11-N15)	15.46	0.50	0.111	LP(O38)	π* (C39-C41)	16.10	0.29	0.087
LP(O53)	π* (C43-C48)	14.32	0.29	0.082	LP(O53)	π* (C44-O54)	15.92	0.29	0.086
LP(N59)	π*(C56-O79)	30.13	0.31	0.125	LP(O54)	σ* (C44-O53)	20.45	0.42	0.118
LP(O79)	σ*(C56-C57)	13.39	0.51	0.106	LP(N59)	π* (C60-C61)	14.13	0.28	0.081
LP(F81)	π*(C4-C5)	16.55	0.33	0.097	LP(O79)	σ*(C56-N59)	13.83	0.66	0.123
π*(C43-C48)	π*(C40-C42)	61.12	0.01	0.062	π*(C43-C48)	π*(C46-C49)	90.84	0.01	0.077
π*(C60-O61)	π*(C62-C65)	80.55	0.02	0.077	π*(C60-C61)	π*(C63-C67)	88.82	0.02	0.080

(C60-C61) and π*(C63-C67), π*(C60-O61) and π*(C62-C65), and π(C43-C48) and π*(C40-C42) with respective highest stabilization energies 90.84, 88.82, 80.55 and 61.12 kcal/mol respectively. The other interactions include LP(N59) to π*(C56-O79), LP(O54) to σ*(C44-O53) and LP(O18) to σ* (C7-N17) with stabilization energies 30.13, 20.45 and 16.53 kcal/mol respectively. Detailed data is given in Supplementary Table 3.

The NHOs, natural hybrid orbitals are a result of symmetrically orthogonalized hybrid orbital, which is derived from the natural atomic orbital (NAO) centred on particular atom *via* unitary transformation. Looking at the simple bond orbital picture, an NBO is defined as an orbital formed from NHOs. The NBO for a localized σ-bond between atoms A and B, is defined as:

$$\sigma_{AB=} c_A h_A \; + \; c_B h_B$$

where h_A and h_B are the natural hybrids centred on atoms A and B and c_A and c_B are the polarization coefficients for atoms A and B.

The parameters spherical polar angles theta (θ) and phi (φ) from the nucleus and the deviation angle *Dev* from the line of the centres between the bonded nuclei specify the direction of each hybrid. In general, for the $sp^\lambda d^\mu$ hybrids, the hybrid direction is numerically determined corresponding to maximum angular amplitude. Further, it is compared with the direction of internuclear axis to determine the magnitude of bending in the bond as the deviation angle between them.

Carbons of σCO/N are more bent away from the line of C_{11}-O_{19}, C_{58}-O_{67}, C_{57}-O_{67} and C_7-N_{17}, C_7-O_{18} centres by 14.9°, 8.2°, 7.3°, 7.3° and 8.3° respectively, as a result of conjugative effect of strong charge transfer and steric effect. Little lower bending effect of 5.9° is also noticed at the C_1-C_{10} group for compound **10a** (Supplementary Table 4).

Similarly, for compound **12a** the carbons are bent away from the line of C_1-C_6 centres by 16.3° while C_{11}-O_{19} centre deviates by 6.9° (Supplementary Table 5).

Molecular Electrostatic Potential

The 3D MEP plots are a useful tool to establish relationship between molecular structure and its physicochemical property. It helps to display molecular size, positive, negative and neutral electrostatic potential regions with the help of color grading. Therefore, 3D MEP plots calculations for these six hybrids were done at B3LYP/6-311G (d,p) level of computation and plots are shown in Figure 13 and 14 and Supplementary Figures S1-S4. The positive electrostatic potential represents proton repulsion by atomic nuclei due to low electron density (blue shades). Similarly, the negative potential represents the proton attraction due to excess electron density (red shades).[32–33] The potential values are represented in varied colors and increase in the order red < orange < yellow < green < blue. The color code of these maps is in the range −0.209 (deepest red) to 0.209 (deepest blue) for **10a-c** and −0.169 to 0.169 for **12a-c** where red and blue represent strongest attraction and repulsion respectively.
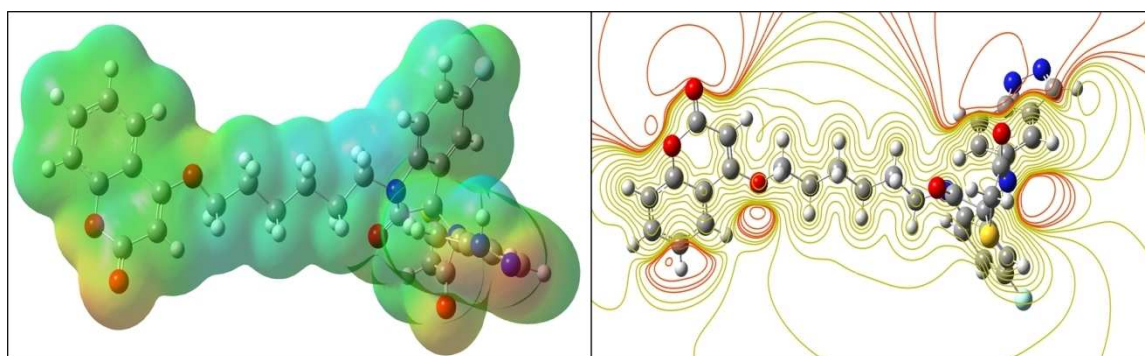
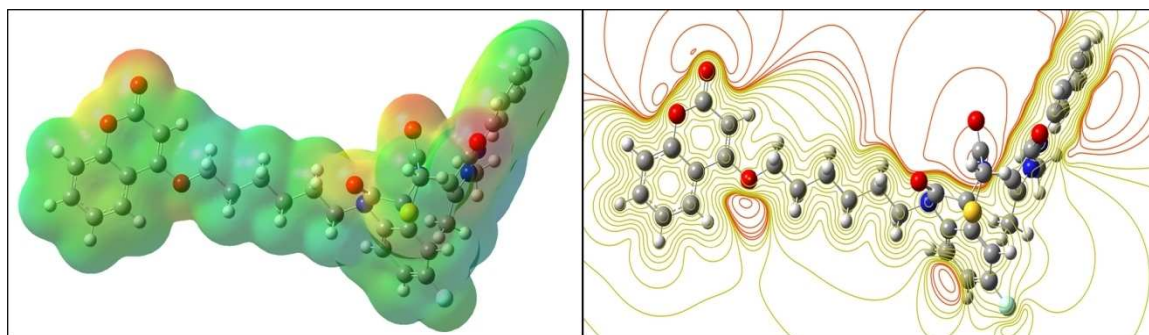**Figure 13.** MEP and contour plot for compound **10a**

Figure 14. MEP and contour plot for compound **12a**

The ESP plots clearly show that the maximum positive region (blue) is located on the alkyl chain due to hydrogen atoms. The maximum negative region (red) is localized on the spiro-indole ring system containing heteroatoms as well as the coumarin ring oxygen. It also indicates that electron donating ability is favorable from them.

A contour plot is a 2D XY plot of a 3D XYZ surface which displays lines at intersection point of surface and planes of constant elevation (Z). The contour plots depict lines of constant density or brightness, such as electrostatic potentials and are drawn in the molecular plane. The electron rich red lines are around heteroatoms whereas the electron deficient region is shown by greenish-yellow lines. The calculations are done at the at 0.004 density values.

The MEP and contour plots are in correlation with the docking interactions which reveal that heteroatoms form pi-cation, pi donor and classical H bonds with G-quadruplex. The coumarin ring with electron donating ability as suggested by MEP and contour plots also forms H bond with G-quadruplex DNA.

Conclusion

Six new spiro indole-coumarin hybrids **10a-c** and **12a-c** have been successfully synthesized using heterocyclic amines through six new Schiff bases. The detailed spectroscopic analysis revealed the true structures of the compounds. Binding interaction of about 22 compounds including these hybrids with DNA G-quadruplex of the human genome, was screened using Molecular docking studies. Compound **10a** was evidenced to be the best ligand with the highest binding energy value of −8.23 kcal/mol. Also, all these hybrid compounds have shown good bioactivity scores and drug likeliness properties. The DFT studies showed high chemical reactivity of all six hybrids through HOMO and LUMO plots. The position of molecular orbitals reveals the charge transfer within the molecule. The detailed NBO analysis of **10a** and **12a**, their MEP plots, hyperconjugative interactions and charge delocalization calculations verified the reactivity and stability of these compounds. However, hybrid **10a** on the basis of global reactivity descriptors filtered to be chemically more reactive than other compounds. The *in vitro* studies for the screened

potential hybrid coumarin derivatives are underway in collaboration.

Supporting Information Summary

Experimental section, Spectroscopic data, complete NBO and NHO tables of **10a** and **12a** and additional molecular electrostatic potential and contour plots are available in supplementary information.

Conflict of Interest

The authors declare no conflict of interest.

Keywords: Coumarin hybrids · G-quadruplexes · molecular docking · NBO analysis · virtual screening

[1] C. Zdero, F. Bohlmann, J. Solomon, *Phytochemistry* **1988**, *27*, 891–897.

[2] R. S. A. de Araujo, J. M. Barbosa-Filho, M. T. Scotti, L. Scotti, R. M. D. da Cruz, V. dos S Falcão-Silva, J. P. de Siqueira-Júnior, F. J. B. Mendonça-Junior, *Scientifica* **2016**, *2016*, Article ID 6894758.

[3] T. Nasr, S. Bondock, M. Youns, *Eur. J. Med. Chem.* **2014**, *9*, 539–548.

[4] X. H. Liu, H. F. Liu, J. Chen, Y. Yang, B. A. Song, L. S. Bai, J. X. Liu, H. L. Zhu, X. B. Qi, *Bioorg. Med. Chem. Lett.* **2010**, *20*, 25705–5708.

[5] L. R. Chen, Y. C. Wang, Y. W. Lin, S. Y. Chou, S. F. Chen, L. T. Liu, Y. T. Wu, C. J. Kuo, T. S. S. Chen, S. H. Juang, *Bioorg. Med. Chem. Lett.* **2005**, *15*, 3058–3062.

[6] J. Amato, N. Iaccarino, B. Pagano, R. Morigi, A. Locatelli, A. Leoni, M. Rambaldi, P. Zizza, A. Biroccio, E. Novellino, A. Randazzo, *Front. Chem.* **2014**, *2*, 54.

[7] R. F. George, S. S. Panda, E. M. Shalaby, A. M. Srour, A. I. S. Farag, A. S. Girgis, *RSC Adv.* **2016**, *6*, 45434–45451.

[8] P. R. Kamath, D. Sunil, A. Ajees, K. S. R. Pai, S. Das, *Bioorg. Chem.* **2015**, *63*, 101–109.

[9] P. R. Kamath, D. Sunil, M. M. Joseph, A. Ajees, A. A. A. Salam, T. T. Sreelekha, *Eur. J. Med. Chem.* **2017**, *136*, 442–451.

[10] M. S. Almutairi, A. Z. Zakaria, P. P. Ignasius, R. R. Al-Wabli, I. H. Joe, M. I. Attia, *J. Mol. Struct.* **2018**, *1153*, 333–345.

[11] P. Khanna, L. Khanna, S. J. Thomas, A. M. Asiri, S. S. Panda, *Curr. Org. Chem.* **2018**, *22*, 67–84.

[12] P. Khanna, S. S. Panda, P. Khanna, S. C. Jain, *Mini-Rev. Org. Chem.* **2014**, *11*, 73–86.

[13] R. Sakhuja, S. S. Panda, L. Khanna, S. Khurana, S. C. Jain, *Bioorg. Med. Chem. Lett.* **2011**, *21*, 5465–5469.

[14] P. Khanna, A. Saxena, L. Khanna, S. Bhagat, S. C. Jain, *Arkivoc.* **2009**, *vii*, 119–125.

[15] M. Jain, R. Sakhuja, P. Khanna, S. Bhagat, S. C. Jain, *Arkivoc* **2008**, *xv*, 54–64.

[16] S. C. Jain, P. Khanna, S. Bhagat, M. Jain, R. Sakhuja, *Phosphorus Sulfur Silicon Relat. Elem.* **2005**, *180*, 1829–1839.

[17] J. Li, X. Jin, L. Hu, J. Wang, Z. Su, *Bioorg. Med. Chem. Lett.* **2011**, *21*, 6969–6972.

[18] S. Haider, *J. Indian Inst. Sci.* **2018**, *98*, 325–339.

[19] F. Moraca, J. Amato, F. Ortuso, A. Artese, B. Pagano, E. Novellino, S. Alcaro, M. Parrinello, V. Limongelli, *Proc. Natl. Acad. Sci. U.S.A.* **2017**, *114*, E2136–E2145.

[20] A. D. Becke, *Phys. Rev. A.* **1988**, *38*, 3098–3100.

[21] C. Lee, W. Yang, R. G. Parr, *Phys. Rev. B.* **1988**, *37*, 785–789.

[22] M. J. Frisch, G. W. Trucks, H. B. Schlegel, G. E. Scuseria, M. A. Robb, J. R. Cheeseman, G. Scalmani, V. Barone, B. Mennucci, G. A. Petersson, H. Nakatsuji, M. Caricato, X. Li, H. P. Hratchian, A. F. Izmaylov, J. Bloino, G. Zheng, J. L. Sonnenberg, M. Hada, M. Ehara, K. Toyota, R. Fukuda, J. Hasegawa, M. Ishida, T. Nakajima, Y. Honda, O. Kitao, H. Nakai, T. Vreven, J. A. Montgomery Jr., J. E. Peralta, F. Ogliaro, M. Bearpark, J. J. Heyd, E. Brothers, K. N. Kudin, V. N. Staroverov, R. Kobayashi, J. Normand, K. Raghavachari, A. Rendell, J. C. Burant, S. S. Iyengar, J. Tomasi, M. Cossi, N. Rega, J. M. Millam, M. Klene, J. E. Knox, J. B. Cross, V. Bakken, C. Adamo, J. Jaramillo, R. Gomperts, R. E. Stratmann, O. Yazyev, A. J. Austin, R. Cammi, C. Pomelli, J. W. Ochterski, R. L. Martin, K. Morokuma, V. G. Zakrzewski, G. A. Voth, P. Salvador, J. J. Dannenberg, S. Dapprich, A. D. Daniels, Ö. Farkas, J. B. Foresman, J. V. Ortiz, J. Cioslowski, D. J. Fox, Gaussian 09; Gaussian Inc.: (Wallingford, CT) **2009**.

[23] R. Dennington, T. Keith, J. Millam, Gauss View, Version 5, Semichem Inc., (Shawnee Mission, KS) **2009**.

[24] G. M. Morris, R. Huey, W. Lindstrom, M. F. Sanner, R. K. Belew, D. S. Goodsell, A. J. Olson, *J. Comput. Chem.* **2009**, *30*, 2785–2791.

[25] F. S. D. Leva, E. Novellino, A. Cavalli, M. Parrinello, V. Limongelli, *Nucleic Acids Res.* **2014**, *42*, 5447–5455.

[26] T. A. Koopmans, *Physica.* **1933**, *1*, 104–113.

[27] R. G. Parr, W. Yang, *Density-functional theory of atoms and molecules*, Oxford University Press, Oxford **1989**.

[28] R. G. Pearson, *J. Org. Chem.* **1987**, *52*, 2131–2136.

[29] R. Meenakshi, *J. Mol. Struct.* **2017**, *1127*, 694–707.

[30] A. E. Reed, F. Weinhold, *J. Chem. Phys.* **1985**, *83*, 1736–1740.

[31] M. Szafran, A. Komasa, E. B. Adamska, *J. Mol. Struct.* **2007**, *827*, 101–107.

[32] P. Politzer, S. J. Landry, T. Warnheim, *J. Phys. Chem.* **1982**, *86*, 4787–4771.

[33] S. Mishra, D. Chaturvedi, N. Kumar, P. Tandon, H. W. Siesler, *Chem. Phys. Lipids* **2010**, *163*, 207–217.